

# Nagaoka ferromagnetism observed in a quantum dot plaquette

<https://doi.org/10.1038/s41586-020-2051-0>

Received: 23 May 2019

Accepted: 8 January 2020

Published online: 2 March 2020

 Check for updates

J. P. Dehollain<sup>1,2,7,8</sup>, U. Mukhopadhyay<sup>1,2,8</sup>, V. P. Michal<sup>1,2</sup>, Y. Wang<sup>3</sup>, B. Wunsch<sup>3</sup>, C. Reichl<sup>4</sup>, W. Wegscheider<sup>4</sup>, M. S. Rudner<sup>5,6</sup>, E. Demler<sup>3</sup> & L. M. K. Vandersypen<sup>1,2</sup>✉

Engineered, highly controllable quantum systems are promising simulators of emergent physics beyond the simulation capabilities of classical computers<sup>1</sup>. An important problem in many-body physics is itinerant magnetism, which originates purely from long-range interactions of free electrons and whose existence in real systems has been debated for decades<sup>2,3</sup>. Here we use a quantum simulator consisting of a four-electron-site square plaquette of quantum dots<sup>4</sup> to demonstrate Nagaoka ferromagnetism<sup>5</sup>. This form of itinerant magnetism has been rigorously studied theoretically<sup>6–9</sup> but has remained unattainable in experiments. We load the plaquette with three electrons and demonstrate the predicted emergence of spontaneous ferromagnetic correlations through pairwise measurements of spin. We find that the ferromagnetic ground state is remarkably robust to engineered disorder in the on-site potentials and we can induce a transition to the low-spin state by changing the plaquette topology to an open chain. This demonstration of Nagaoka ferromagnetism highlights that quantum simulators can be used to study physical phenomena that have not yet been observed in any experimental system. The work also constitutes an important step towards large-scale quantum dot simulators of correlated electron systems.

The potential impact of discovering and understanding exotic forms of magnetism and superconductivity is one of the main motivations for research in condensed-matter physics. These quantum mechanically governed effects result from the strong correlations that arise between interacting electrons. Modelling and simulating such systems can, in some instances, be achieved only through the use of engineered, controllable systems that operate in the quantum regime<sup>1</sup>. Efforts to build quantum simulators have already shown great promise at this early stage<sup>10</sup>, mainly led by the ultracold-atom community<sup>11–17</sup>. More broadly, quantum simulations of many-body fermionic systems have been carried out in a range of experimental systems, such as quantum dot lattices<sup>18</sup>, dopant atoms<sup>19</sup>, superconducting circuits<sup>20</sup> and trapped ions<sup>21</sup>.

Electrostatically defined semiconductor quantum dots<sup>22–24</sup> have been proposed as excellent candidates for quantum simulations<sup>25–27</sup>. Their ability to reach thermal energies far below the hopping and on-site interaction energies enables access to previously unexplored material phases. Quantum dot systems have already achieved success in realizing simulations of Mott-insulator physics in linear arrays<sup>28</sup>. In addition, the feasibility to extend these systems into two-dimensional (2D) lattices has recently been demonstrated<sup>4,29–32</sup>, including the ability to perform measurements of spin correlations<sup>4</sup>. As a result, quantum dot systems are now prime candidates for exploring how superconductivity and magnetism emerge in strongly correlated electron systems<sup>33–35</sup>.

The emergence of magnetism in purely itinerant electron systems is a long-standing problem in quantum many-body physics<sup>2,3</sup>, with only a few rigorous theoretical results, for instance, in systems with special flat bands or Nagaoka's ferromagnetism (see ref. <sup>36</sup> and references therein). The Nagaoka model of ferromagnetism<sup>5,37</sup> relies on the simplicity of the Hubbard model<sup>38</sup>, which captures complex correlations between electrons in a lattice with only two Hamiltonian parameters. Using this single-band model, Nagaoka proved analytically that for some lattice configurations, and in the limit of infinitely strong interactions, the presence of a single hole on top of a Mott-insulating state with one electron per site renders the ground state ferromagnetic. The Nagaoka mechanism can be intuitively understood as an interference effect between the different paths that the hole can take across the lattice. These paths interfere constructively when all lattice sites have the same spin orientation, which lowers the kinetic energy of the hole.

Given that Nagaoka obtained his rigorous result using unrealistic limits, it has been an open question whether this mechanism can still be responsible for the observation of ferromagnetism in an experimental, finite-size system, in the presence of long-range interactions and disorder, as well as additional available orbitals. In this light, we note that a ferromagnetic state is a fully polarized spin state, and as such is an eigenstate of the total spin operator  $S_{\text{tot}}^z$ . This statement is true whether the system is in the thermodynamic limit or whether it is finite size. The feasibility of performing a quantum simulation of

<sup>1</sup>QuTech, TU Delft, Delft, The Netherlands. <sup>2</sup>Kavli Institute of Nanoscience, TU Delft, Delft, The Netherlands. <sup>3</sup>Department of Physics, Harvard University, Cambridge, MA, USA. <sup>4</sup>Solid State Physics Laboratory, ETH Zürich, Zürich, Switzerland. <sup>5</sup>Center for Quantum Devices, Niels Bohr Institute, University of Copenhagen, Copenhagen, Denmark. <sup>6</sup>Niels Bohr International Academy, Niels Bohr Institute, University of Copenhagen, Copenhagen, Denmark. <sup>7</sup>Present address: School of Mathematical and Physical Sciences, University of Technology Sydney, Sydney, New South Wales, Australia. <sup>8</sup>These authors contributed equally: J. P. Dehollain, U. Mukhopadhyay. ✉e-mail: l.m.k.vandersypen@tudelft.nl

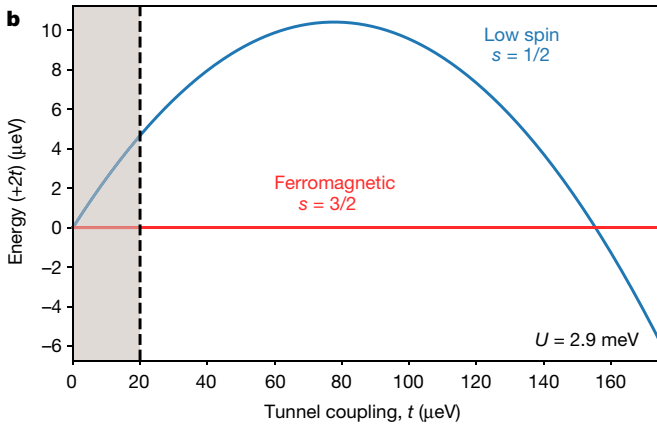
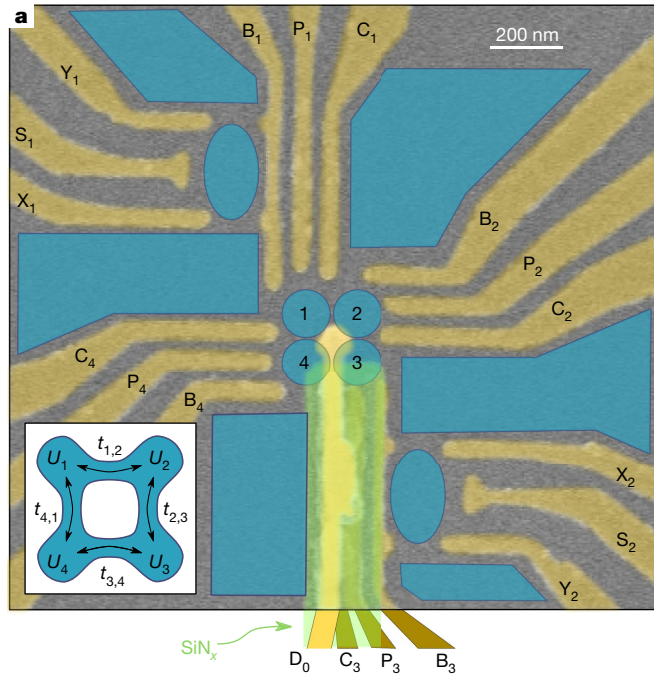


**Fig. 1 | Device schematic and Nagaoka model.** **a**, False-coloured scanning electron microscope image of a device from the same batch as the one used in the experiments. The gate structure used to define the quantum dots is coloured in dark gold. A slab of silicon nitride (coloured in green) is laid over gates  $C_3$  and  $P_3$  to electrically isolate those gates from the  $D_0$  gate (coloured in bright gold), which runs over them and contacts the substrate at the centre of the structure. Overlaid in blue is a sketch of the expected 2D electron gas density, showing the four dots forming a plaquette in the centre of the device, along with nearby charge sensors and electron reservoirs. Inset: schematic of the plaquette showing the relevant tunnel couplings and on-site interaction energies. **b**, Energy spectrum as a function of tunnel coupling using the solution expressed in equation (2), with  $U = 2.9$  meV. The shaded area shows the experimentally accessible range of  $t$  in this system.

Nagaoka ferromagnetism has been explored theoretically for quantum dots<sup>6–8</sup> as well as optical superlattices<sup>9</sup>, but there are no experimental reports to date.

Here we present clear experimental evidence of Nagaoka ferromagnetism, using a quantum dot device designed to host a  $2 \times 2$  array of electrons. Using the high degree of parameter tunability, we study how external magnetic fields and disorder in local potentials affect the magnetic nature of the ground state. Furthermore, by effectively tuning the geometry of the system from periodic to open boundary conditions, we experimentally demonstrate the suppression of ferromagnetism expected from the Lieb–Mattis theorem<sup>39</sup>.

## Nagaoka in the quantum dot plaquette

The single-band Hubbard model provides a simple description of interacting electrons in a lattice, such as the plaquette of electrostatically defined and controlled quantum dots (Fig. 1a). The Hamiltonian contains competing kinetic energy and electron–electron interaction terms:

$$H_H = - \sum_{\langle i,j \rangle \sigma} t_{ij} c_{i\sigma}^\dagger c_{j\sigma} + \sum_i U_i n_{i\uparrow} n_{i\downarrow} - \sum_i \mu_i n_i \quad (1)$$

where  $t_{ij}$  describes electron tunnelling between sites  $i$  and  $j$ ,  $U_i$  is the on-site Coulomb repulsion energy at site  $i$  and  $\mu_i$  is a local energy offset at site  $i$ . In typical quantum dot systems,  $U_i$  is mainly set by the geometry of the device and is on the order of 1 meV, while  $t_{ij}$  and  $\mu_i$  can be controlled by gate voltages in the range of 0 to 0.5 meV and 0 to 20 meV, respectively<sup>27</sup>. The operators  $c_{i\sigma}$ ,  $c_{i\sigma}^\dagger$  and  $n_{i\sigma}$  represent the second quantization annihilation, creation and number operators for an electron on site  $i$  with spin projection  $\sigma = \{\uparrow, \downarrow\}$ .

Nagaoka ferromagnetism is predicted to occur with an almost-half-filled lattice, which for the case of the  $2 \times 2$  plaquette corresponds to having three interacting electrons in the four-site system. By additionally restricting the system to nearest-neighbour-only coupling, the Hamiltonian is analytically solvable<sup>6</sup> for homogeneous interactions ( $U_i = U$ ,  $t_{ij} = t$ ,  $\mu_i = 0$ ) and in the limit  $U \gg t$ , where the lowest eigenenergies are:

$$E_{3/2} = -2t \text{ and } E_{1/2} = -\sqrt{3}t - \frac{5t^2}{U} \quad (2)$$

Here  $E_{3/2}$  is the energy of the high-spin, ferromagnetic quadruplets (with total spin  $s = 3/2$ ) and  $E_{1/2}$  is the energy of the two sets of low-spin  $s = 1/2$  degenerate doublets (see Supplementary Methods for details).

We note that the Hamiltonian in equation (1) neglects some of the essential features of the experimental device used in this work. For comparison with experimental results, we employ a more general model Hamiltonian, in which we account for interdot Coulomb repulsion (in Fig. 2a), spin–orbit and hyperfine interactions (in Extended Data Figs. 3, 4a), and the effects of external magnetic fields. The implementation of these terms is described in detail in the Supplementary Methods. In addition to this model, we have also performed an ab initio calculation (see Supplementary Methods, Extended Data Figs. 5, 6, and ref. 40) based on multiple orbitals solved from a potential landscape with  $2 \times 2$  minima, which shows similar results to those obtained with equation (1).

The simple model described by equations (1) and (2) already provides some useful insight into the parameter regimes relevant to the experiment. The ferromagnetic state is the ground state at large  $U/t$ , with a transition to a low-spin ground state occurring at  $U/t = 18.7$ . The quantum dot array used in this work has an average  $U \approx 2.9$  meV, with tunable nearest-neighbour tunnel couplings in the range of  $0 < t < 20$   $\mu$ eV (ref. 4). Unless otherwise stated, we set  $t_{i,i+1} \approx 16$   $\mu$ eV. This means that we are probing the regime where the ground state is expected to be ferromagnetic (Fig. 1b).

We prepare the system by using charge stability diagrams<sup>41</sup> to find the appropriate voltage bias that will stabilize the system in a charge configuration with three resonant electrons delocalized in the four sites. We set the local energy reference at this regime as  $\mu_i(N) = 0$  eV for all dots, and refer to this condition as point N. Charge stability diagrams are also used to tune the gates to the measurement point M, where single-shot measurements in the singlet–triplet ( $|S\rangle - |T\rangle$ ) basis are performed on two of the three electrons. Figure 2a and Extended Data Fig. 1 show simulated and measured charge stability diagrams where points N and M can be identified, along with an inset schematic of the dot local energies at these points.

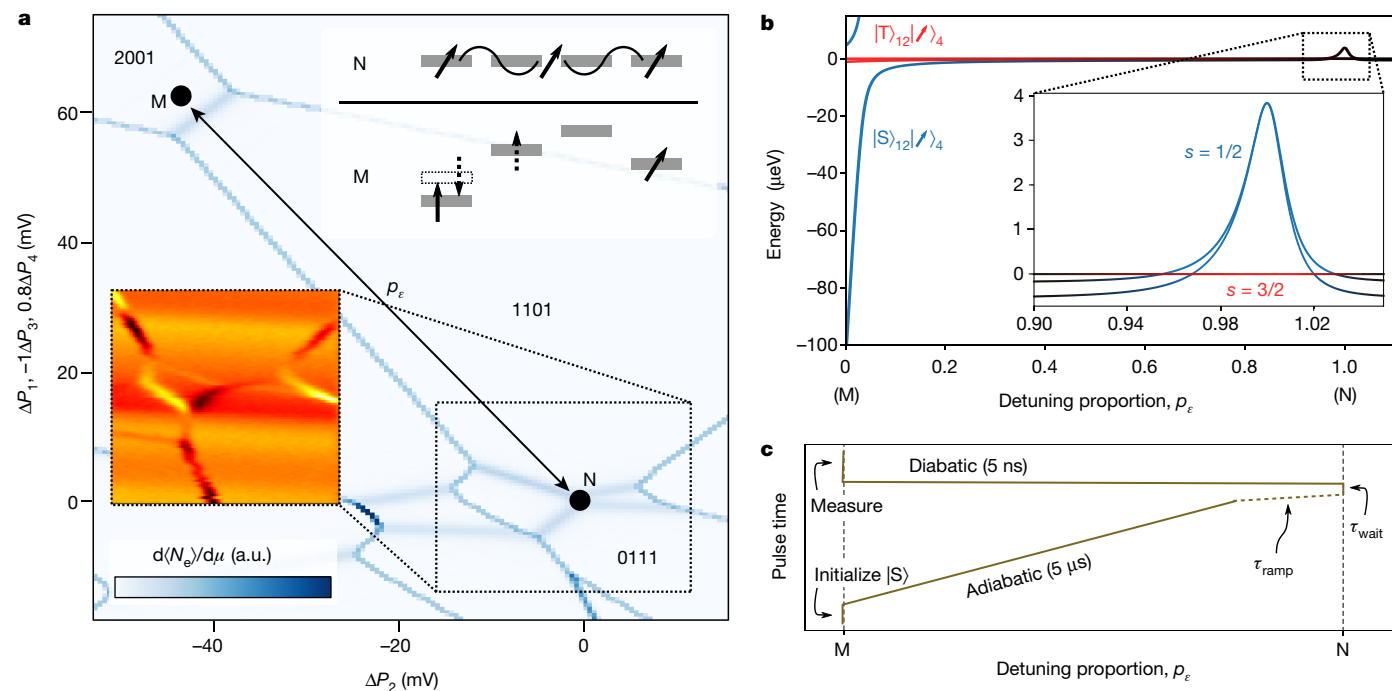


**Fig. 2 | Experimental protocol.** **a**, Simulated charge stability diagram plotting the change in electron occupation  $N_e$  in the approximate gate space used in the experiment. In the experiment, we pulse in a straight line in gate space from point M to point N and back. The top-right inset shows a schematic of the local energies at points N and M, highlighting in the latter how the measurement of two spins in the singlet-triplet basis is performed through spin-to-charge conversion. The bottom-left inset shows a measured charge stability diagram of the dotted region, with the same gate voltage ratios as the simulation, which we use in the experiment to calibrate the gate voltages at point N. **b**, Calculated energy spectrum as a function of  $p_\epsilon$ , using the theoretical model (equation (1)

With the accessible system parameters, the theoretically expected (Fig. 1b) energy gap between the ferromagnetic ( $s = 3/2$ ) and low-spin ( $s = 1/2$ ) states at point N is  $E_{1/2} - E_{3/2} \approx 4 \mu\text{eV}$ , comparable to the measured thermal energy of about  $6 \mu\text{eV}$  (electron temperature of about  $70 \text{ mK}$ )<sup>4</sup>. To study the magnetic properties of the ground state, we have developed a technique (Fig. 2b, c) based on initializing a low-entropy state at point M and adiabatically pulsing to point N to access the ground state. We then diabatically pulse back to point M and probe the spin state of the system on timescales faster than the relaxation times. By shortening the ramp time  $\tau_{\text{ramp}}$  of the pulse from point M to N, we can also access excited states. To distinguish whether the system is in a ferromagnetic or low-spin state, we repeat the cycle of preparation and measurement, and extract the triplet probability  $\mathcal{P}_T$ , which informs us on the nature of the original three-spin state (see Supplementary Methods for details). In Methods, we provide a detailed description of these preparation and measurement protocols.

### Experimental results

Figure 3 shows plots of  $\mathcal{P}_T$  as we perform measurements at different values of detuning proportion  $p_\epsilon$ , defined as the quantity that sets the linear combination of voltages  $P_i$  on gates  $P_i$  (Fig. 1a) such that at  $p_\epsilon = 1(0)$  the system is tuned to point N(M). In the inset of the figure, we highlight that  $\mathcal{P}_T$  remains at a low value for most of the range, with a sharp increase as  $p_\epsilon$  approaches 1 (point N). This is consistent with the expectation that the electrons will remain localized until the region close to point N, where they begin to delocalize and the  $\mathcal{P}_T$  measurement starts to project the three interacting spins (see Methods for details). This is expected to happen after  $p_\epsilon \approx 0.96$ , where the energy spectrum (inset of

and Supplementary Methods) without spin-coupling effects. Parameters were set to the experimental values presented in Methods. The inset shows a zoomed-in spectrum of the region where the three spins are delocalized on all four dots, where there are a total of eight states: the  $s = 3/2$  quadruplets (red) and the two sets of  $s = 1/2$  doublets (blue), of which one set connects with the  $|T\rangle$  branch and the other with the  $|S\rangle$  branch at point M. Line colours represent the spin state of the system in each region, denoted by the labels in the figure. The energies extracted from the numerical solutions are offset by the energy of  $|s, m\rangle = |3/2, +3/2\rangle$ . **c**, Pulse sequence used in the experiment (see Methods for detailed description).

Fig. 2b) shows an energy-level crossing and the  $s = 3/2$  states become the ground state. The non-zero triplet fraction at low  $p_\epsilon$  is attributed partly to thermal excitations during the initialization stage (Methods)—as a consequence of the finite electron temperature—and partly to a small probability of leakage to excited states during the pulse.

The main plot shows the measurement around point N, for a range of  $\tau_{\text{ramp}}$ . In the region  $0.99 < p_\epsilon < 1.03$ , a clear increase of  $\mathcal{P}_T$  is observed as  $\tau_{\text{ramp}}$  is increased, consistent with a gradual transition from diabatically pulsing into the low-spin state, to adiabatically pulsing into the ferromagnetic state, where  $\mathcal{P}_T$  is maximum. For the faster pulses, we see  $\mathcal{P}_T$  peaks at  $p_\epsilon$  values of 0.99 and 1.03, where the pulse reaches the energy-level crossings, as all the spin states quickly (that is, much faster than the experimental timescales) mix owing to the nuclear hyperfine fields and spin-orbit coupling<sup>42–44</sup>.

The  $\tau_{\text{ramp}}$  timescale for the diabatic to adiabatic transition shown in Extended Data Fig. 4a can be theoretically studied using time-evolution simulations with an extended Hubbard model (see Supplementary Methods for details). From fits to the data, we estimate a hyperfine coupling parameter  $\delta_N = 73 \pm 3 \text{ neV}$ , in agreement with previous observations and calculations in similar GaAs quantum dot systems<sup>44–46</sup>. Extended Data Fig. 4b shows  $\mathcal{P}_T$  as a function of the waiting time  $\tau_{\text{wait}}$  spent at point N ( $p_\epsilon = 1$ ), consistent with thermal equilibration of the system with a timescale  $\tau_{\text{relax}} \approx 2 \mu\text{s}$ .

We note that we cannot directly assign the measured values of  $\mathcal{P}_T$  to  $s = 1/2$  and  $s = 3/2$  populations, because the observed  $\mathcal{P}_T$  is subject to measurement imperfections caused by mechanisms that are difficult to disentangle, such as the finite measurement bandwidth, the signal-to-noise ratio and  $|T\rangle$  to  $|S\rangle$  relaxation, as well as unwanted leakage to other states during the pulsed passages.



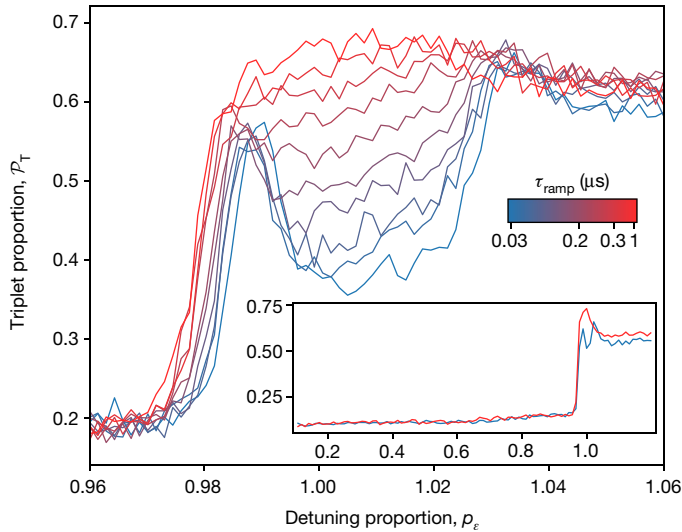


**Fig. 3 | Main signature of Nagaoka ferromagnetism.** Measured  $\mathcal{P}_T$  versus  $p_e$  using the protocol described in the main text (10,000 repetitions per point in each curve). Different curves correspond to different values of  $\tau_{\text{ramp}}$ . The main figure focuses on the region close to point N, while the inset is zoomed out to the entire detuning range for the two extreme values of  $\tau_{\text{ramp}}$ .  $\tau_{\text{wait}}$  is fixed to 50 ns (500 ns) for the main figure (inset).

### Changing topology from 2D to 1D

Whereas the square plaquette can be thought of as a 1D ring, the Lieb–Mattis theorem<sup>6,39</sup> asserts that the ground state of a 1D array of electrons with open boundary conditions has the lowest possible spin. We can intuitively understand the difference between these two configurations when we consider how the hole tunnels to its next-nearest neighbour<sup>3</sup>. In a 2D plaquette, the hole has two possible paths to the next-nearest neighbour, the two paths will leave the system in two different spin configurations. However, for an  $s = 3/2$  system, the two paths leave identical spin configurations, and interfere constructively to lower the kinetic energy. In contrast, in an open-boundary 1D array, the kinetic energy of the hole is independent of the spin configurations of the neighbouring electrons as there is only one path for the hole through the array.

One powerful feature of the quantum dot system is that the tunnel barriers can be tuned independently, allowing us to test different array topologies. In Fig. 4a, we compare diabatic and adiabatic sweeps as we raise the tunnel barrier that controls  $t_{23}$ , effectively transforming the plaquette into a system that behaves more like an open-boundary 1D system. In the latter regime, we see that  $\mathcal{P}_T$  becomes insensitive to sweep rate. In addition, we no longer observe the peaks of  $\mathcal{P}_T$  for the fast sweep rate, which we had associated with mixing at the avoided level crossings. From these observations, we infer that for the open chain, the instantaneous ground state does not exhibit an avoided crossing between an  $s = 1/2$  state and an  $s = 3/2$  state as the system is taken to point N. In this regime, the  $p_e$  sweeps will always evolve to the  $s = 1/2$  ground state, independent of the sweep rate. This interpretation is also consistent with the numerical simulations of the energy spectrum shown in Fig. 4b.

### Effects of external magnetic fields

Given that Nagaoka ferromagnetism originates from interference effects due to the trajectories of the hole around the ring, it then follows that a magnetic flux through the plaquette will add an Aharonov–Bohm phase<sup>47</sup> that disturbs the interference effects. We capture this effect in the theoretical model by adding a magnetic-field-dependent gauge to the tunnelling term in equation (1). In addition, the application of an external field subjects the system to the Zeeman effect, causing a spin-dependent energy offset. See Supplementary Methods for details

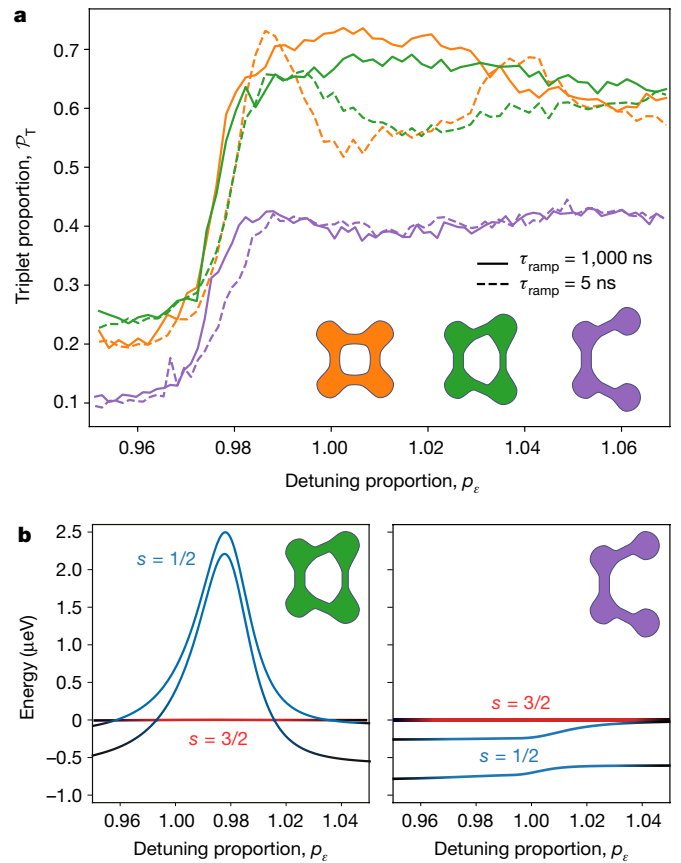
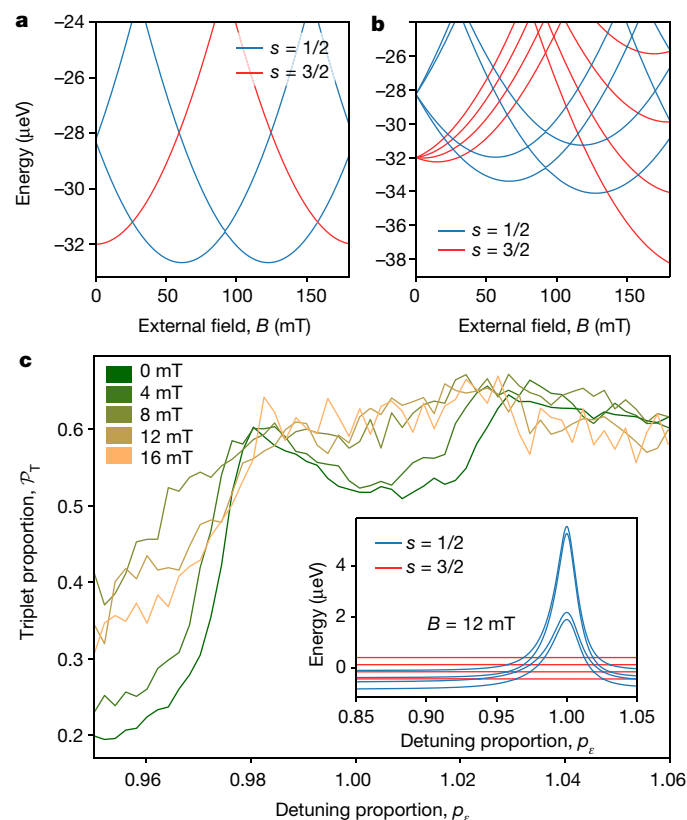


**Fig. 4 | From ring to chain.** **a**, Comparison of three measurements with the following values of tunnel couplings [ $t_{1,2}, t_{2,3}, t_{3,4}, t_{4,1}$ ] (in  $\mu\text{eV}$ ): [19(1), 15(1), 17(2), 19(5)] (orange); [16(1), 7.9(5), 20(2), 19(2)] (green); [18(4), 0.0, 21(1), 21(3)] (purple). The offsets in  $\mathcal{P}_T$  between the curves are not attributed to the topology, but are due to small measurement-to-measurement variations in the thermal excitation rate during the initialization stage of the protocol. **b**, Calculated energy spectrum as a function of  $p_e$ , using the tunnel coupling values corresponding to the green (left) and purple (right) plots from **a**.

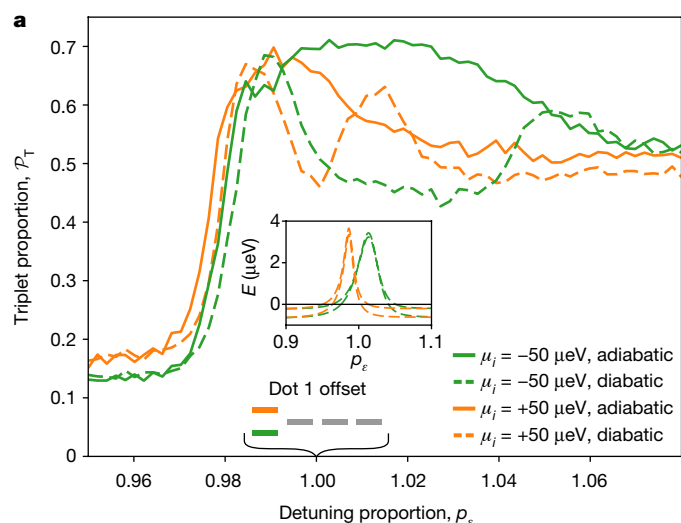
on how the gauge and Zeeman terms are implemented in the extended Hubbard model.

Figure 5a shows the effect of a magnetic field  $B$  through the plaquette on the spectrum, ignoring the Zeeman effect. The lowest  $s = 1/2$  and  $s = 3/2$  levels at point N are shown as a function of the applied field, where periodic crossings can be observed. In the range  $30 < B < 160$  mT, the system ground state transitions to the low-spin state, with the perhaps counterintuitive implication that we can destroy the ferromagnetic state by applying a magnetic field. In addition, this effect highlights that the ferromagnetic state in this system is dominated by the Nagaoka effect rather than long-range interactions. In line with this observation, the ab initio calculations suggest that long-range interactions only account for about 20% of the ferromagnetic polarization<sup>40</sup>. When we include the Zeeman effect (Fig. 5b), the picture becomes more complicated, because both Zeeman and orbital effects cause perturbations of similar energy scales.

From this initial numerical analysis, it is clear that the experimental characterization of the effect of the external field will be challenging, owing to the increased complexity of the spectral structure of the spin states as a function of field. The small energy splittings that appear both at point N, as well as at lower  $p_e$  values (inset of Fig. 5c) are expected to cause mixing of the spin states during the adiabatic pulses. To minimize this mixing, we adjusted the pulsing protocol such that we pulse adiabatically (1  $\mu\text{s}$  ramp) to  $p_e = 0.2$ , then pulse diabatically (5 ns ramp) the rest of the way. The results in Fig. 5c show that from 4 to 8 mT,  $\mathcal{P}_T$  increases at point N, and we stop observing the characteristic



**Fig. 5 | Applying an external magnetic field.** **a**, Lowest eigenenergies of the  $s = 1/2$  (blue) and  $s = 3/2$  (red) states at point N as a function of magnetic field, obtained from the numerical model after including the effect of an Aharonov–Bohm phase. **b**, Same as **a** but with the addition of the Zeeman effect, and the lowest four eigenenergies of each  $s$  states are shown. **c**, Experimental measurement using diabatic passage, for different fields in the range of 0 to 16 mT. The inset shows a numerically calculated spectrum at 12 mT, with the Aharonov–Bohm phase and Zeeman effect included in the model.



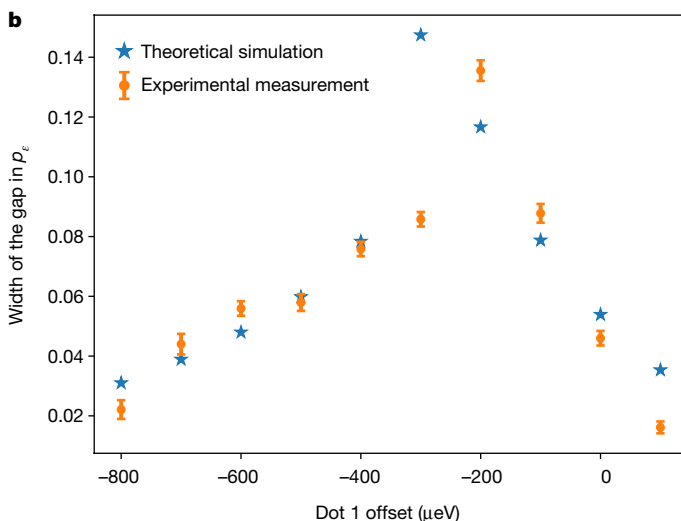
**Fig. 6 | Local energy offsets.** **a**, Experimental measurements with a similar protocol used to probe the states at point N, but pulsing instead to a point N', where the local energy of dot 1 is offset by  $\pm 50 \mu\text{eV}$ . The inset shows numerically calculated spectra for the same experimental condition. **b**, Comparison between the experimentally measured and theoretically simulated ranges in

dip. Note that the range of field that we were able to probe is still below the estimated ground state transition point (about 30 mT). Therefore, we infer that the observed increase in  $\mathcal{P}_T$  results from hybridization of the  $s = 1/2$  and  $s = 3/2$  states as their energy gap reduces. We cannot claim that the observed hybridization of states is occurring solely at point N, as it is evident from the increase in  $\mathcal{P}_T$  at  $p_e < 0.97$  (that is, before the energy-level crossings) that some of the mixing is occurring during the pulse. However, we do see that  $\mathcal{P}_T$  in all plots converges at the energy-level crossings ( $p_e \approx 0.97$  and  $p_e \approx 1.03$ ), suggesting that the Aharonov–Bohm orbital effects are partly responsible for the additional mixing near point N. Attempts to perform the measurement at higher fields closer to the expected spin-state transition resulted in similar plots.

### Sensitivity to local energy offsets

We also use the tunability available in quantum dot systems to study the effects of disorder of the local potential. For the plot in Fig. 6a, we modified the experimental protocol used to probe the states at point N, pulsing instead to a point N', where the local energy of dot 1 is offset by  $\pm 50 \mu\text{eV}$ . We achieve this by employing the virtual gates technique<sup>4,28</sup>, which gives access to control knobs that map a linear combination of  $P_i$  gates onto local dot energy offsets. The measurements show that the region in the detuning trajectory where the ferromagnetic state is the ground state changes in width and position when different offsets are applied. The panel inset shows the expected energy spectra when we simulate the experimental conditions using the model in equation (1). The spectra show excellent qualitative agreement with the measured variations in width and position of the gapped region. In Extended Data Fig. 7, we repeated the measurement on each of the four dots, showing similar qualitative agreement with theory.

Figure 6b compares experimental measurements and theoretical predictions of the width of the detuning proportion region (as defined in the caption of Extended Data Fig. 8) with a ferromagnetic ground-state energy gap, for offsets of dot 1 in the range  $+100$  to  $-800 \mu\text{eV}$ . This plot further confirms the interpretation of the experimental observations, showing excellent agreement between measurements and theoretical predictions. Remarkably, the system still shows signs of the ferromagnetic ground state with offsets up to  $-400 \mu\text{eV}$  (Extended Data Fig. 8), more than an order of magnitude larger than the tunnel coupling. We also note that the theoretical simulations in Extended Data Fig. 8 suggest



detuning proportion where the  $s = 3/2$  to  $s = 1/2$  gap is visible. The points used to determine the widths in both experimental measurements and theoretical simulations are shown in Extended Data Fig. 8. Error bars are calculated from the fits to the peaks used to determine the widths from the experimental data.

that from  $-500 \mu\text{eV}$ , the ground state is no longer  $s = 3/2$ , even though the measurement still shows a gap in  $\mathcal{P}_T$  between diabatic and adiabatic sweeps. The presence of this gap is explained by the large splitting between the two  $s = 1/2$  branches that occurs at such large local offsets.

## Discussion

In this work, we have presented measurements showing experimental evidence of Nagaoka's 50-year-old theory in a small-scale system. The large degree of tunability, high ratio of interaction strength to temperature and fast measurement techniques available to quantum dot systems allowed the observation of both the ferromagnetic ground state and the low-spin excited state of an almost-half-filled lattice of electrons. By performing a quantum simulation involving both charge and spin, we have built on previous demonstrations<sup>28</sup> showing that quantum dot systems can be useful simulators of the extended Hubbard model, despite their initial inhomogeneities in the potential shape and local energies. Furthermore, we have shown a flavour of the capabilities for studying the sensitivity to disorder, and these experiments have already revealed some remarkable effects, when we found that the Nagaoka condition can still be observed after offsetting a local energy by amounts much larger than the tunnel coupling. This can readily be studied in further detail, along with other possibilities for exploring the effects of disorder, which could bring insights into, for example, the stability of the ferromagnetic state. More quantitative insight of the energy gap between the spin states can be achieved through spectroscopy measurements, using techniques such as applying oscillating electric fields through a gate<sup>48</sup> or observing 'exchange-like' oscillations<sup>49</sup>.

While the problem of three electrons in a four-site plaquette can be solved analytically using the single-band Hubbard picture, a complete description of this experimental system that includes all its available orbitals is not easily tractable, analytically or numerically. Indeed, the computational cost of the ab initio calculation of the five lowest states, with long-range and on-site interaction terms being considered, is on the order of 10,000 CPU hours. Small-scale simulations on tractable models can be used to systematically benchmark the performance of devices as the scale-up technology develops towards devices that can perform classically intractable simulations. Larger quantum dot systems (or other experimentally controllable systems), such as ladders or two-dimensional arrays can shed more light on the existence of purely itinerant ferromagnetism in real systems. The exchange interaction grows proportionally to the system size, creating a competition against the hopping energy that is characteristic of Nagaoka ferromagnetism, and leaving the fate of the Nagaoka mechanism in larger systems unknown.

## Online content

Any methods, additional references, Nature Research reporting summaries, source data, extended data, supplementary information, acknowledgements, peer review information; details of author contributions and competing interests; and statements of data and code availability are available at <https://doi.org/10.1038/s41586-020-2051-0>.

1. Feynman, R. P. Simulating physics with computers. *Int. J. Theor. Phys.* **21**, 467–488 (1982).
2. Auerbach, A. *Interacting Electrons and Quantum Magnetism* (Springer, 1994).
3. Mattis, D. C. *The Theory of Magnetism Made Simple* (World Scientific, 2006).
4. Mukhopadhyay, U., Dehollain, J. P., Reichl, C., Wegscheider, W. & Vandersypen, L. M. K. A  $2 \times 2$  quantum dot array with controllable inter-dot tunnel couplings. *Appl. Phys. Lett.* **112**, 183505 (2018).
5. Nagaoka, Y. Ferromagnetism in a narrow, almost half-filled s band. *Phys. Rev.* **147**, 392–405 (1966).
6. Mattis, D. C. Eigenvalues and magnetism of electrons on an artificial molecule. *Int. J. Nanosci.* **02**, 165–170 (2003).
7. Nielsen, E. & Bhatt, R. N. Nanoscale ferromagnetism in nonmagnetic doped semiconductors. *Phys. Rev. B* **76**, 161202(R) (2007).
8. Oguri, A., Nisikawa, Y., Tanaka, Y. & Numata, T. Kondo screening of a high-spin Nagaoka state in a triangular quantum dot. *J. Magn. Magn. Mater.* **310**, 1139–1141 (2007).
9. von Stecher, J., Demler, E., Lukin, M. D. & Rey, A. M. Probing interaction-induced ferromagnetism in optical superlattices. *New J. Phys.* **12**, 055009 (2010).

10. Georgescu, I. M., Ashhab, S. & Nori, F. Quantum simulation. *Rev. Mod. Phys.* **86**, 153–185 (2014).
11. Trotzky, S. et al. Time-resolved observation and control of superexchange interactions with ultracold atoms in optical lattices. *Science* **319**, 295–299 (2008).
12. Nascimbène, S. et al. Experimental realization of plaquette resonating valence-bond states with ultracold atoms in optical superlattices. *Phys. Rev. Lett.* **108**, 205301 (2012).
13. Bloch, I., Dalibard, J. & Nascimbène, S. Quantum simulations with ultracold quantum gases. *Nat. Phys.* **8**, 267–276 (2012).
14. Dai, H.-N. et al. Four-body ring-exchange interactions and anyonic statistics within a minimal toric-code Hamiltonian. *Nat. Phys.* **13**, 1195–1200 (2017).
15. Görg, F. et al. Enhancement and sign change of magnetic correlations in a driven quantum many-body system. *Nature* **553**, 481–485 (2018).
16. Salomon, G. et al. Direct observation of incommensurate magnetism in Hubbard chains. *Nature* **565**, 56–60 (2019); correction **566**, E5 (2019).
17. Nichols, M. A. et al. Spin transport in a Mott insulator of ultracold fermions. *Science* **363**, 383–387 (2019).
18. Singha, A. et al. Two-dimensional Mott-Hubbard electrons in an artificial honeycomb lattice. *Science* **332**, 1176–1179 (2011).
19. Salfi, J. et al. Quantum simulation of the Hubbard model with dopant atoms in silicon. *Nat. Commun.* **7**, 11342 (2016).
20. Barends, R. et al. Digital quantum simulation of fermionic models with a superconducting circuit. *Nat. Commun.* **6**, 7654 (2015).
21. Martinez, E. A. et al. Real-time dynamics of lattice gauge theories with a few-qubit quantum computer. *Nature* **534**, 516–519 (2016).
22. Kouwenhoven, L. P., Austing, D. G. & Tarucha, S. Few-electron quantum dots. *Rep. Prog. Phys.* **64**, 701–736 (2001).
23. van der Wiel, W. G. et al. Electron transport through double quantum dots. *Rev. Mod. Phys.* **75**, 1–22 (2002).
24. Hanson, R., Kouwenhoven, L. P., Petta, J. R., Tarucha, S. & Vandersypen, L. M. K. Spins in few-electron quantum dots. *Rev. Mod. Phys.* **79**, 1217–1265 (2007).
25. Manousakis, E. A quantum-dot array as model for copper-oxide superconductors: a dedicated quantum simulator for the many-fermion problem. *J. Low Temp. Phys.* **126**, 1501–1513 (2002).
26. Byrnes, T., Kim, N. Y., Kusudo, K. & Yamamoto, Y. Quantum simulation of Fermi-Hubbard models in semiconductor quantum-dot arrays. *Phys. Rev. B* **78**, 075320 (2008).
27. Barthelemy, P. & Vandersypen, L. M. K. Quantum dot systems: a versatile platform for quantum simulations. *Ann. Phys.* **525**, 808–826 (2013).
28. Hensgens, T. et al. Quantum simulation of a Fermi-Hubbard model using a semiconductor quantum dot array. *Nature* **548**, 70–73 (2017).
29. Thalineau, R. et al. A few-electron quadruple quantum dot in a closed loop. *Appl. Phys. Lett.* **101**, 103102 (2012).
30. Seo, M. et al. Charge frustration in a triangular triple quantum dot. *Phys. Rev. Lett.* **110**, 046803 (2013).
31. Noiri, A. et al. A triangular triple quantum dot with tunable tunnel couplings. *Semicond. Sci. Technol.* **32**, 084004 (2017).
32. Mortemousque, P.-A. et al. Coherent control of individual electron spins in a two dimensional array of quantum dots. Preprint at <http://arxiv.org/abs/1808.06180v1> (2018).
33. Scalapino, D. J. The case for  $d_{x^2-y^2}$  pairing in the cuprate superconductors. *Phys. Rev.* **250**, 329–365 (1995).
34. Tsuei, C. C. & Kirtley, J. R. Pairing symmetry in cuprate superconductors. *Phys. Rev. B* **72**, 969–1016 (2000).
35. Balents, L. Spin liquids in frustrated magnets. *Nature* **464**, 199–208 (2010).
36. Tasaki, H. From Nagaoka's ferromagnetism to flat-band ferromagnetism and beyond: An introduction to ferromagnetism in the Hubbard model. *Prog. Theor. Phys.* **99**, 489–548 (1998).
37. Thouless, D. J. Exchange in solid  $^3\text{He}$  and the Heisenberg Hamiltonian. *Planet. Space Sci.* **86**, 893–904 (1965).
38. Hubbard, J. Electron correlations in narrow energy bands. *Proc. R. Soc. A* **276**, 238–257 (1963).
39. Lieb, E. & Mattis, D. Theory of ferromagnetism and the ordering of electronic energy levels. *Phys. Rev.* **125**, 164–172 (1962).
40. Wang, Y. et al. Ab initio exact diagonalization simulation of the Nagaoka transition in quantum dots. *Phys. Rev. B* **100**, 155133 (2019).
41. van der Wiel, W. G., Stopa, M., Koder, T., Hatano, T. & Tarucha, S. Semiconductor quantum dots for electron spin qubits. *New J. Phys.* **8**, 28 (2006).
42. Khaetskii, A. V., Loss, D. & Glazman, L. Electron spin decoherence in quantum dots due to interaction with nuclei. *Phys. Rev. Lett.* **88**, 186802 (2002).
43. Merkulov, I. A., Efros, A. L. & Rosen, M. Electron spin relaxation by nuclei in semiconductor quantum dots. *Phys. Rev. B* **65**, 205309 (2002).
44. Chekhovich, E. A. et al. Nuclear spin effects in semiconductor quantum dots. *Nat. Mater.* **12**, 494–504 (2013).
45. Petta, J. R. Coherent manipulation of coupled electron spins in semiconductor quantum dots. *Science* **309**, 2180–2184 (2005).
46. Koppens, F. H. L. Control and detection of singlet-triplet mixing in a random nuclear field. *Science* **309**, 1346–1350 (2005).
47. Aharonov, Y. & Bohm, D. Significance of electromagnetic potentials in the quantum theory. *Phys. Rev.* **115**, 485–491 (1959).
48. Nowack, K. C., Koppens, F. H. L., Nazarov, Y. V. & Vandersypen, L. M. K. Coherent control of a single electron spin with electric fields. *Science* **318**, 1430–1433 (2007).
49. Malinowski, F. K. et al. Spin of a multielectron quantum dot and its interaction with a neighboring electron. *Phys. Rev. X* **8**, 011045 (2018).

**Publisher's note** Springer Nature remains neutral with regard to jurisdictional claims in published maps and institutional affiliations.

© The Author(s), under exclusive licence to Springer Nature Limited 2020

### Device fabrication

The experiment was performed using an array of four gate-defined quantum dots in a  $2 \times 2$  geometry<sup>4</sup>. The device substrate consists of an AlGaAs/GaAs heterostructure, designed to have a 2D electron gas 90 nm below the surface. The quantum dots are defined and controlled using metallic gates patterned on the surface of the substrate, as shown in the scanning electron microscope image of a device from the same batch as the one used in this work in Fig. 1a. We employed a double-layer gate structure to form this dot array. The first layer of gates—which includes all gates except  $D_0$ —was created using electron-beam lithography, evaporation and lift-off of Ti/Au with 5/20 nm thickness. We then fabricate a  $1.5 \times 0.2 \mu\text{m}$  dielectric slab on top of the gates  $C_3$  and  $P_3$ , using electron-beam lithography, sputtering and lift-off of SiN<sub>x</sub> with a thickness of 50 nm. Finally, the  $D_0$  gate is created using the same process as the other gates, with 10/100-nm-thick Ti/Au. This gate runs over the gate  $C_3$  before contacting the substrate at the centre of the dot array. The gates created in the first layer are 30-nm wide, whereas the width of the  $D_0$  gate is 100 nm.

### Device operation and calibration of experimental parameters

The full set of gates  $B_i$ ,  $P_i$ ,  $C_i$  and  $D_0$  shown in Fig. 1a are designed to define and control the quantum dot plaquette. In addition, gates  $X_i$ ,  $Y_i$  and  $S_i$  define two larger quantum dots, which are used as charge sensors. Different parameters of the dot array can be controlled using voltages on different gates. The  $P_i$  gates are designed to control the electron filling of dot  $i$  by adjusting the dot chemical potential  $\mu_i$ . Gates  $D_0$  and  $C_i$  are designed to control the tunnel coupling  $t_{ij}$ , while gates  $B_i$  and  $C_{i+1}$  are designed to control the coupling between dot  $i$  and its reservoir. In reality, the proximity between the gates causes non-negligible cross-capacitances, complicating independent control of the parameters that the gates were designed to control. For some of the tuning stages, we make use of linear combinations of gate voltages—known as virtual gates<sup>4,28</sup>—to provide a direct experimental knob to Hamiltonian parameters such as  $\mu_i$  and  $t_{ij}$ .

We use charge stability diagrams<sup>23</sup> to identify the charge state of the system as a function of different  $P_i$  voltages. We can convert changes in gate voltages  $\Delta P_i$  into changes in dot local offset energies  $\Delta\mu_i$  by measuring the lever arms  $\alpha_i = \Delta\mu_i/\Delta P_i$ , using the method described in detail in ref.<sup>28</sup>. For this device, the measured values are  $\alpha_{[1,2,3,4]} = [30(2), 45(4), 55(6), 38(3)] \mu\text{eV mV}^{-1}$ . The uncertainty in the estimation of  $\alpha_i$  is dominated by the precision with which we can identify a charge transition in the charge stability diagram, which is about 1 mV. Different features of the charge stability diagrams are also used to estimate the effective Hamiltonian parameters in the experimental system<sup>4,28</sup>. The effective on-site interaction  $U_i$  is measured by extracting the local energy offset in dot  $i$  required to change the occupation from one electron to two electrons. For this device, these values were measured to be  $U_{[1,2,3,4]} = [2.9(2), 2.6(2), 2.9(3), 3.0(2)] \text{ meV}$ . The uncertainty in the estimation of  $U_i$  is calculated from the vector sum of the relative uncertainties of the roughly 1 mV measurement precision, and the uncertainty in  $\alpha_i$  used in the conversion from voltage to energy. The effective tunnel coupling term  $t_{ij}$  is measured by analysing the width of the step in the charge sensing signal as the detuning between dots  $i$  and  $j$  is swept to transfer a single electron between them. For most of the results in this work, the  $t_{ij}$  terms were tuned to  $16(4) \mu\text{eV}$ . The uncertainty in  $t_{ij}$  has roughly equal contributions from the estimation of the coupling from the fit to the width of the step and the ability to simultaneously tune all four couplings. For the results in Fig. 4,  $t_{2,3}$  was tuned to different values, which are provided in the figure caption. The charge stability diagram simulations (Fig. 2a), require values for the interdot Coulomb repulsion  $V_{ij}$ , which are also extracted from measured charge stability diagrams as  $V_{1,2} = 0.47(6) \text{ meV}$ ,  $V_{2,3} = 0.35(7) \text{ meV}$ ,  $V_{3,4} = 0.43(7) \text{ meV}$ ,  $V_{1,4} = 0.30(4) \text{ meV}$ ,  $V_{1,3} = 0.28(6) \text{ meV}$ ,  $V_{2,4} = 0.18(5) \text{ meV}$ .

We make use of charge stability diagrams to observe charge tunnelling events either between an electron reservoir and a dot, or between two dots in the plaquette. These diagrams (such as the ones in Fig. 2a, Extended Data Figs. 1, 2) allow us to map out the charge occupation of the system as a function of voltage in the gates.

To observe signatures of Nagaoka ferromagnetism, we need to tune the system to a regime where it is loaded with three electrons, and the charge configuration energies of the electrons are resonant. We set the local energy reference at this regime as  $\mu_i(N) = 0 \text{ eV}$  for all dots, and refer to this condition as point N (Fig. 2a).

To tune  $t_{i,i+1}$  close to point N, we first localize two of the electrons in dots  $i+2$ ,  $i+3$  (that is, by slightly lowering  $\mu_{i+2}, \mu_{i+3}$ ), and keep dots  $i$ ,  $i+1$  resonant using the remaining electron to measure their tunnel coupling. Here we use cyclic dot indices with  $i = \{1, 2, 3, 4\}$ .

Since the sensing dots are only sensitive to charge tunnelling events, a spin-to-charge conversion protocol<sup>24</sup> is needed to perform measurements of the spin state of the system. We do this at point M, where  $\mu_i^M \approx [-2.5, 0.0, 1.0, -0.5] \text{ meV}$  (inset of Fig. 2a). There, the ground charge state is  $[2, 0, 0, 1]$  (where  $[n_1, n_2, n_3, n_4]$  corresponds to the number of electrons with dot number in the subscript), while the first excited charge state is  $[1, 1, 0, 1]$ . These states have an uncoupled spin in dot 4, with the remaining two spins in a singlet (S) (triplet (T)) configuration for the ground (first excited) state. We chose to use dots 1 and 2 for readout, because we obtained the highest readout contrast from this pair of dots in this device.

The exact gate voltages required to tune the device to points M and N need to be calibrated visually using charge stability diagrams. In Extended Data Fig. 1b, we show a sample charge stability diagram similar to the ones used to identify the gate voltages that will tune the device to point M. After the initial visual calibration, we fine-tune the gate voltages to maximize the  $|T\rangle$  to  $|S\rangle$  relaxation time, which was in the range of 30 to 50  $\mu\text{s}$  in this device. We characterize the thermal excitation rate at point M by analysing the observed random telegraph signal, in which the spins spend about 10 to 20% of the time in the triplet state, consistent with the values measured at small  $p_e$  seen in the inset of Fig. 3.

Point N was also calibrated visually, using charge stability diagrams such as those in Extended Data Fig. 2. We note that the scale of the  $t_{ij}$  terms limit the precision with which we can identify point N, as larger  $t$  broadens the interdot transitions, making them harder to identify in the charge stability diagrams.

Once we have fine-tuned the gate voltages at points M and N, we define a linear combination of  $P_i$  voltages that joins the two points by a straight line in gate voltage space. To do this, we define a virtual gate  $VP_e$  such that a change in the voltage of this gate simultaneously changes all  $P_i$  voltages by different amplitudes, effectively moving the system along the ‘detuning proportion’  $p_e$  axis in Fig. 2b (see also the line along the charge stability diagram in Fig. 2a), defined such that  $\mu_i(p_e) = (1 - p_e)\mu_i^M$ .

To make sure that no unwanted charge transitions are crossed along the  $p_e$  axis, we use charge stability diagrams such as those shown in Fig. 2a (simulated) and Extended Data Fig. 1 (measured), which use a gate combination that allows to see both points N and M in the same diagram.

### Measurement protocol

Figure 2b presents the results of a theoretical simulation showing the lowest three multiplets of the energy spectrum of the three-electron system, along the line that connects point M to point N. Close to point M, we see a typical double quantum dot spectrum corresponding to the  $[2, 0, 0, 1] \leftrightarrow [1, 1, 0, 1]$  charge transition with the  $|S\rangle$  and  $|T\rangle$  branches, while in the region around point N, the spins delocalize and we see branches corresponding to the quadruplets and doublets of the three-electron system.

With this device, we can probe the spin state of the three-electron system using the following protocol: (1) repeatedly (10,000 times)

pulse rapidly from point N to point M; (2) for each repetition, perform single-shot  $|S\rangle/|T\rangle$  measurements using dots 1 and 2 and taking two out of the three electrons; and (3) extract the triplet probability  $\mathcal{P}_T$ . Under ideal conditions, this constitutes a two-spin projective measurement of the three-electron system, resulting in  $\mathcal{P}_T^{(3/2)} = 1$  when the three-electron system is in a ferromagnetic state (any of the  $s = 3/2$  quadruplets). In the low-spin sector ( $s = 1/2$ ), there are two sets of doublet states available, one of which projects two spins to  $|S\rangle$ , while the other projects to  $|T\rangle$  (see Supplementary Methods for details). In this system, the doublets are effectively degenerate (Fig. 2b), and their hybridization will result in  $\mathcal{P}_T^{(1/2)} = 0.5$ .

Owing to the low ratio of energy-level splitting to temperature at point N, we cannot probe the ground state of the system by way of relaxation. Instead, we have developed a technique similar to those previously used in quantum dot<sup>24</sup> and cold atom<sup>11,12,14</sup> systems, where a low-entropy state is evolved coherently to the state of interest. To do this, we apply a gate pulse sequence that follows the detuning range shown in the energy spectrum plotted in Fig. 2b. Using the pulse sequence drawn in Fig. 2c, a two-spin singlet state with a third, free spin sitting on dot 4 is initialized by waiting at point M for 500  $\mu\text{s}$ . Next we apply a pulse on  $VP_\epsilon$  towards point N of amplitude  $p_\epsilon$ . We then wait a time  $\tau_{\text{wait}}$  at  $\mu_i(p_\epsilon)$ , before finally pulsing back to point M to perform the measurement. Importantly, the level crossings seen in Fig. 2b are in fact avoided level crossings with spin-orbit and nuclear hyperfine mediated coupling between the spin states (see Supplementary Methods for details). This avoided level crossing allows to probe the different states in the region around  $p_\epsilon = 1$ , by varying the ramp rate in the pulse sequence: a slow (fast) ramp rate results in an adiabatic (diabatic) passage through the avoided level crossings, so the ground (excited) state is reached. In practice, to minimize leakage to excited states along the way, 80% of the pulse is performed adiabatically, with the variable ramp time  $\tau_{\text{ramp}}$  only applied to the remaining 20%. As long as  $\tau_{\text{wait}}$  is shorter than the thermal relaxation timescale, the measurement of  $\mathcal{P}_T$  will be able to distinguish between high- and low-spin states at point N. To observe relaxation of the  $s = 1/2$  and  $s = 3/2$  states (Extended Data Fig. 4c), we keep  $p_\epsilon = 1$  fixed and vary the wait time  $\tau_{\text{wait}}$  spent at point N.

## Data availability

The datasets obtained from the measurements described in this work are available in the repository Zenodo with the identifier <https://doi.org/10.5281/zenodo.3258940>.

## Code availability

The code used to plot the datasets and implement the models used to reproduce all the figures in the main manuscript is available in the repository Zenodo with the identifier <https://doi.org/10.5281/zenodo.3258940>.

**Acknowledgements** We acknowledge input and discussions with M. Chan, S. Philips, Y. Nazarov, F. Liu, L. Janssen, T. Hensgens, T. Fujita and all of the Vandersypen team, as well as experimental support by L. Blom, C. van Diepen, P. Eendebak, F. van Riggelen, R. Schouten, R. Vermeulen, R. van Ooijik, H. van der Does, M. Ammerlaan, J. Haanstra, S. Visser and R. Roeleveld. L.M.K.V. thanks the NSF-funded MIT-Harvard Center for Ultracold Atoms for its hospitality. This work was supported by grants from the Netherlands Organisation for Scientific Research (FOM projectruimte and NWO Vici) (J.P.D., U.M., L.M.K.V.), the European Research Council (ERC-Synergy) (V.P.M., L.M.K.V.), the Postdoctoral Fellowship in Quantum Science of the Harvard-MPG Center for Quantum Optics and AFOSR-MURI Quantum Phases of Matter (grant number FA9550-14-1-0035) (Y.W.), the Swiss National Science Foundation (C.R., W.W.) and The Villum Foundation (M.S.R.).

**Author contributions** B.W., M.S.R., E.D. and L.M.K.V. had equal contribution in conceptualization. Experimental investigation and methodology was performed with equal contribution from J.P.D. and U.M. Theoretical investigation was led by J.P.D., V.P.M. and B.W. (extended Hubbard models), and Y.W. (ab initio model). J.P.D. led the data curation and software, with support from U.M. and V.P.M. J.P.D. and U.M. had equal contribution in the formal analysis, with support from V.P.M. L.M.K.V. led the funding acquisition and supervision. U.M. led the resources (device fabrication) with support from J.P.D. C.R. and W.W. led the resources (heterostructure growth). J.P.D. led the writing—original draft, with review and editing support from U.M., V.P.M., Y.W., M.S.R., E.D. and L.M.K.V. Please refer to the Casrai Credit Taxonomy for definitions of each of these roles.

**Competing interests** The authors declare no competing interests.

## Additional information

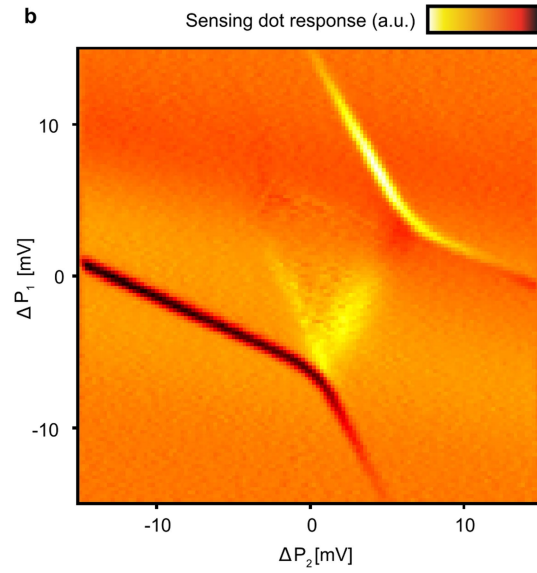
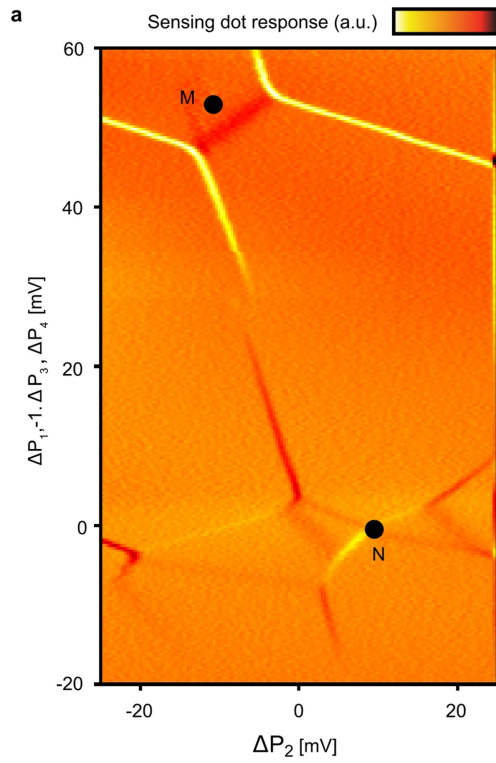
**Supplementary information** is available for this paper at <https://doi.org/10.1038/s41586-020-2051-0>.

**Correspondence and requests for materials** should be addressed to L.M.K.V.

**Peer review information** Nature thanks Joe Salfi, Igor Zutic and the other, anonymous, reviewer(s) for their contribution to the peer review of this work.

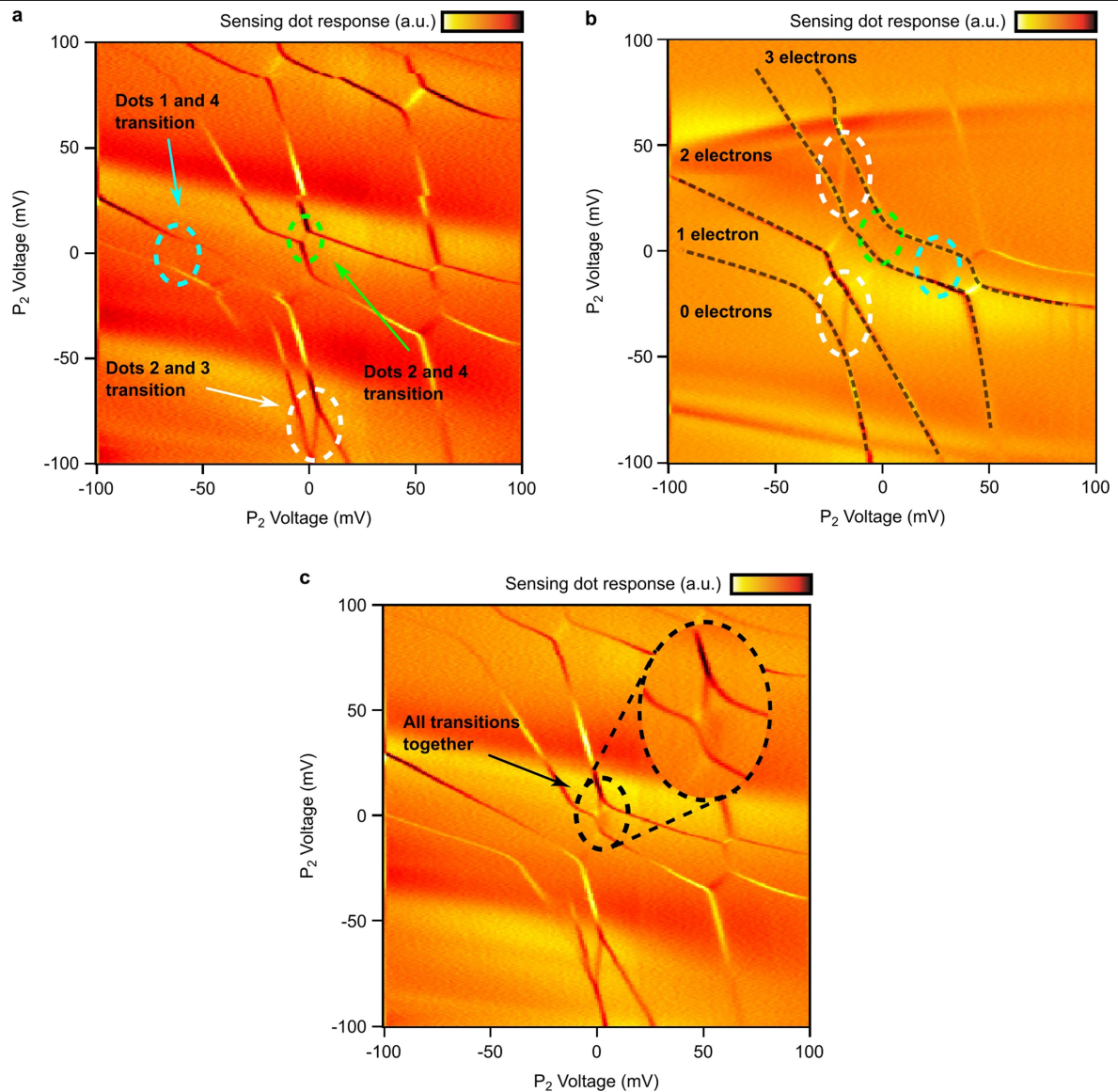
**Reprints and permissions information** is available at <http://www.nature.com/reprints>.





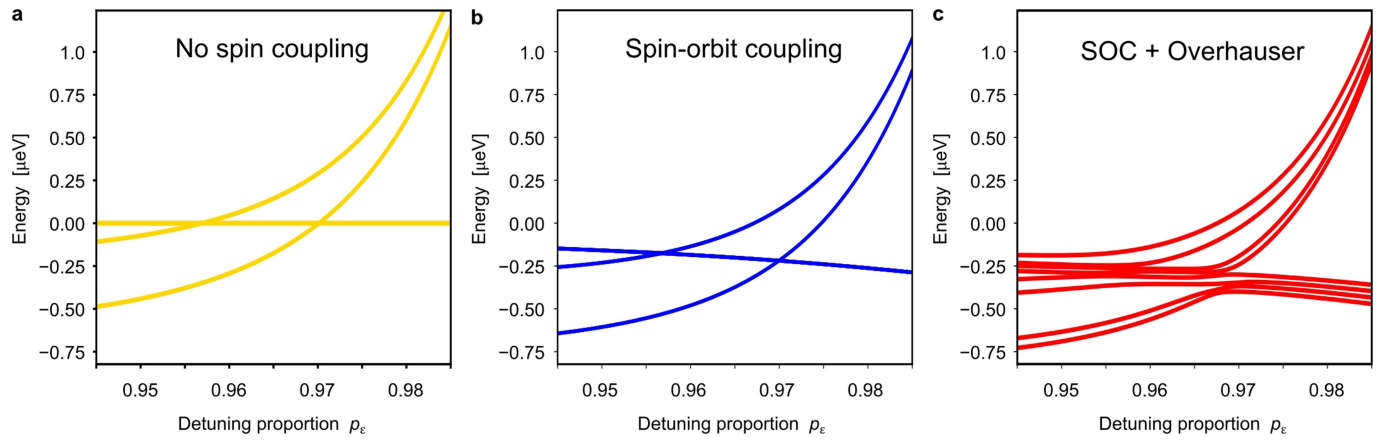
**Extended Data Fig. 1 | Charge stability diagram of the relevant voltage regions. a.** Measured charge stability diagram showing both point N and point M, as highlighted in Fig. 2a. **b.** Measured charge stability diagram focusing on

the 2001:1101 charge transition, where spin measurements are performed (point M).



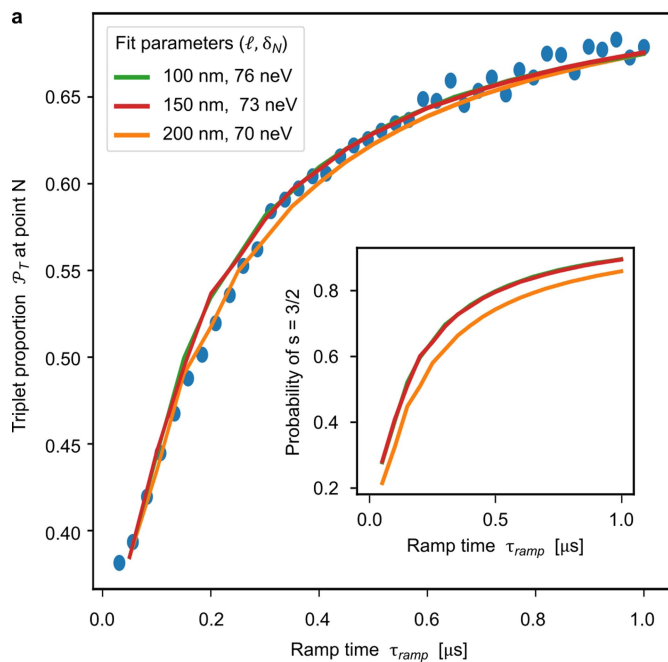
**Extended Data Fig. 2 | Tuning the gate voltages to the Nagaoka condition using charge stability diagrams.** **a**, Sample charge stability diagram where we have highlighted the visible interdot transitions, where the electrochemical potentials of two dots become resonant (that is, an electron is allowed to tunnel between the two dots). **b**, Charge stability diagram similar to **a**, where we have modified gates  $P_1$  and  $P_3$  such that the interdot transitions appear at different locations in the diagram. Dashed black lines delimit the regions with a fixed

total electron occupation in the system. **c**, In this diagram, gates  $P_1$  and  $P_3$  have been tuned to observe the Nagaoka condition, where the three visible interdot transitions are aligned in the three-electron configuration. The intersite interaction in the system provides an effective isolation from the reservoirs for a narrow range of gate voltages, such that the system can remain stable with three electrons in the resonant configuration.



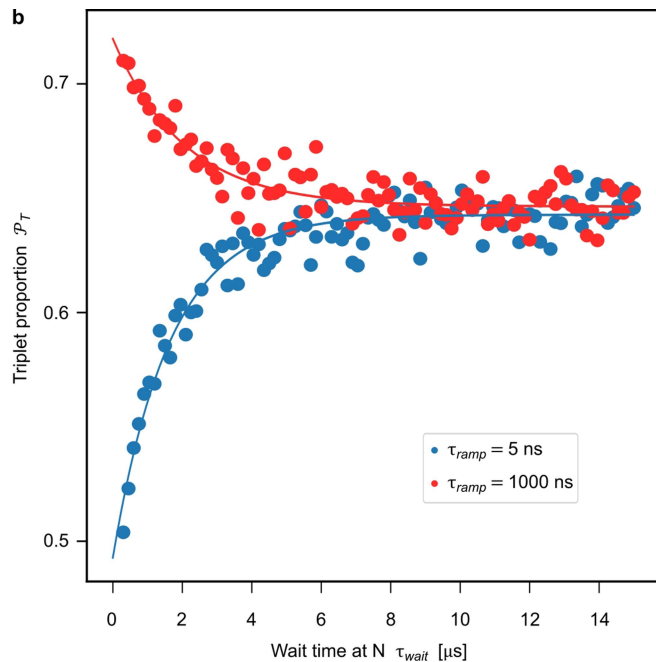
**Extended Data Fig. 3 | Effects of spin-coupling mechanisms.** Calculated spectra of the system in the region of  $p_\epsilon$  close to the level crossing of the  $s=1/2$  and  $s=3/2$  energies, comparing the effects of different mechanisms for spin coupling. **a**, Spectrum without any spin coupling effects. **b**, Spectrum including only spin-orbit coupling (SOC) effects. **c**, Sample spectrum with

both spin-orbit and hyperfine induced Overhauser field gradients, using a single combination of  $h_{\text{Na}}$  fields (as defined in the Supplementary Methods) selected from a normal distribution with standard deviation  $\delta_N = 73$  neV. The Supplementary Methods describe the implementations of these spin-coupling terms in the theoretical model.



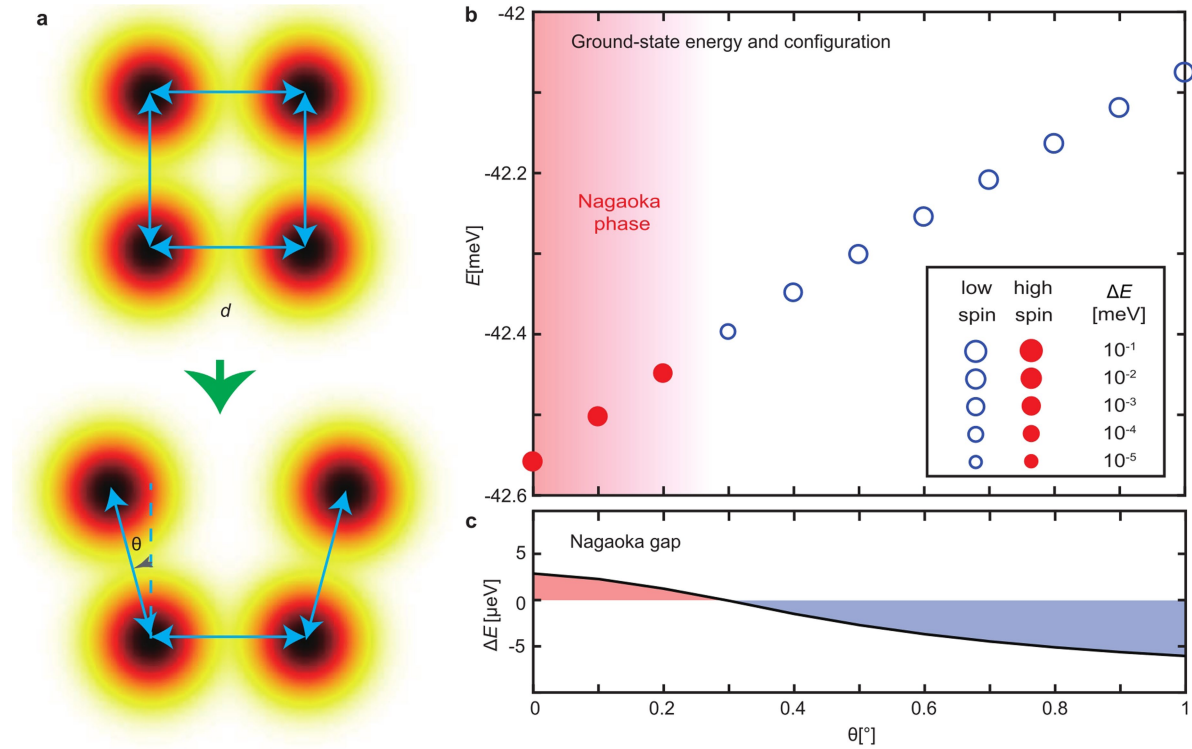
**Extended Data Fig. 4 | Characterization of the Nagaoka condition.**

**a.** Average  $\mathcal{P}_T$  in the detuning region  $1.00 < p_\varepsilon < 1.01$  for 40 values of  $\tau_{ramp}$  within the same range shown in Fig. 3. Solid lines are fits using the time evolution simulations described in the Supplementary Methods, for different values of distance  $\ell$  between neighbouring dots. Inset shows the unscaled results of the



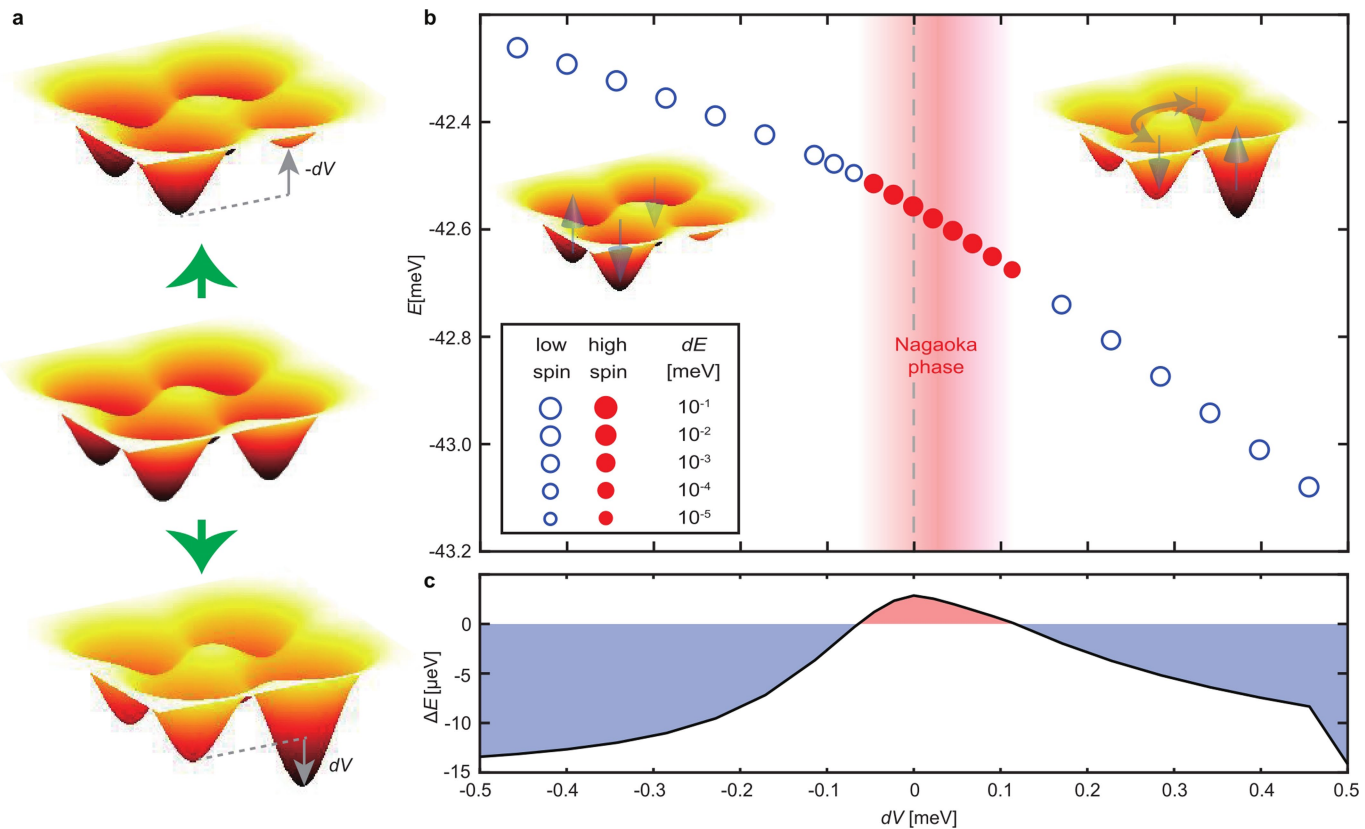
time-evolution simulations, where the probability of  $s = 3/2$  is the sum of the lowest four eigenstate probabilities from the final evolved state. **b.** Thermal relaxation measurements.  $\mathcal{P}_T$  is measured for increasing wait times at point N, for diabatic (blue) and adiabatic (red) passages. Solid lines are exponential fits as guide to the eye.





**Extended Data Fig. 5 | Ab initio simulations from 2D to 1D.** **a**, Schematic of the methodology used in the ab initio simulations to reproduce the effect of the four-dot system transition from a 2D plaquette to a 1D chain. We gradually vary the angle  $\theta$ , which effectively varies the distance between two of the dots. **b, c**,

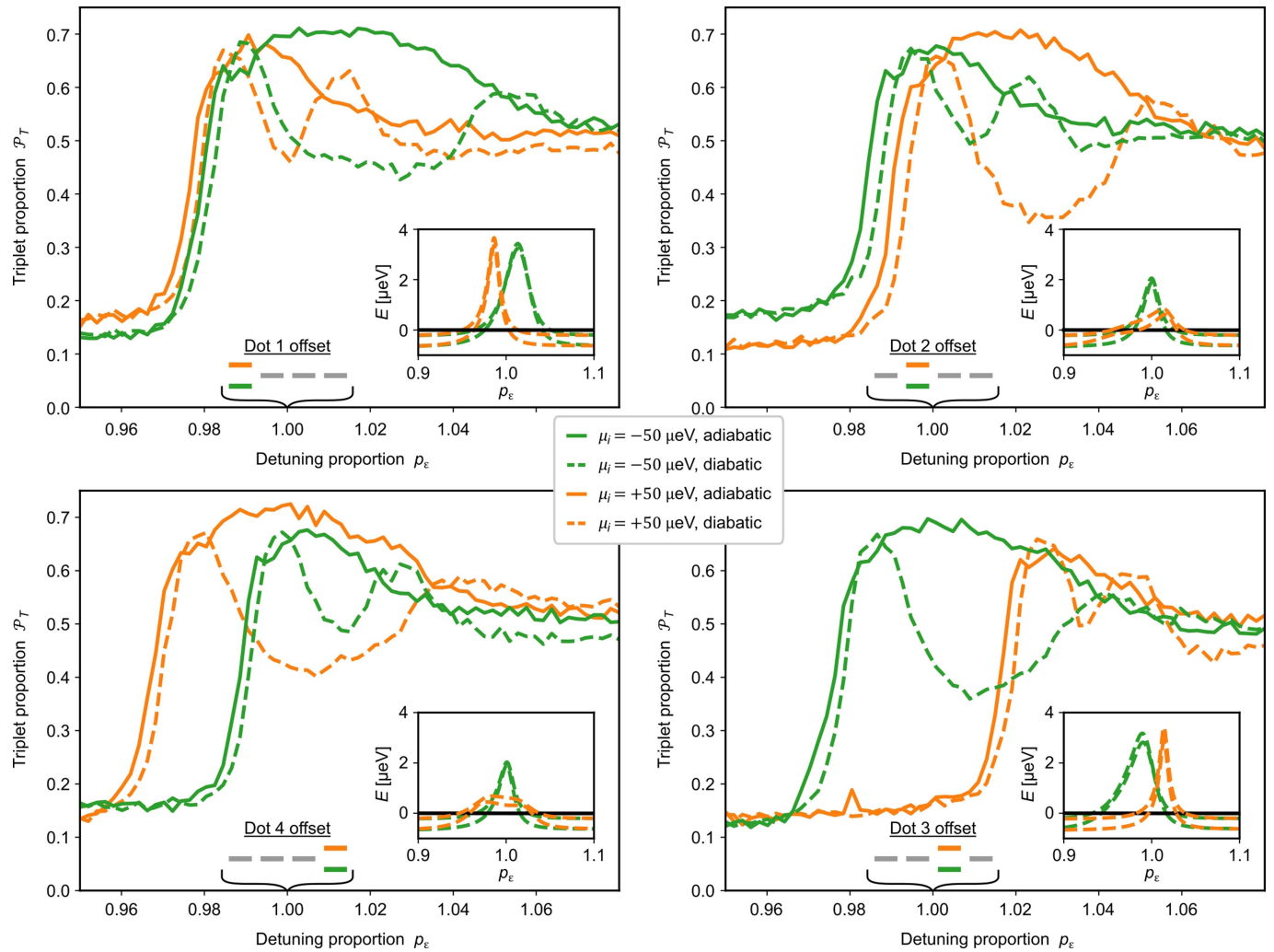
The ground-state energy and spin configuration (**b**) and the ferromagnetic to low-spin energy gap  $\Delta E$  as a function of  $\theta$  (**c**). The ground state soon becomes a low-spin state for the rotating angle at  $0.3^\circ$ .



**Extended Data Fig. 6 | Ab initio simulations for local energy offsets.**

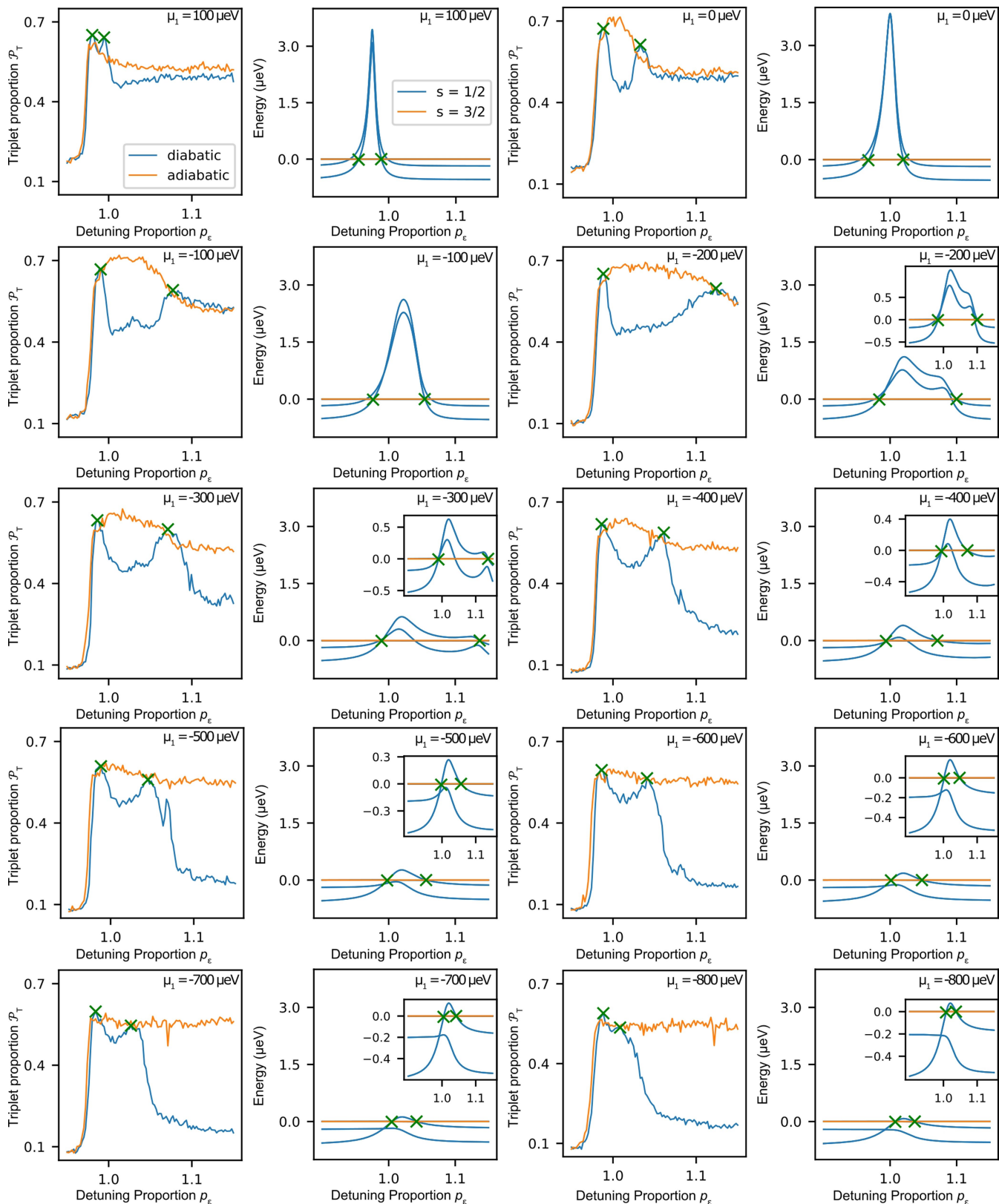
**a**, Schematic of the methodology used in the ab initio simulations to reproduce the effect of a local energy offset. The amplitude of the potential  $V$  of one of the quantum wells is changed by an amount  $dV$ . The variation of the single-well potential by positive or negative  $dV$  gives unbalanced site energies. Besides, with the change of eigenstate basis, the hybridization and interaction parameters are also affected in the ab initio calculation. **b, c**, The ground-state energy and spin configuration (**b**) and the ferromagnetic to low-spin energy

gap  $\Delta E$  as a function of  $dV$  (**c**). When the potential detuning is  $dV = 0.11$  meV or  $dV = -0.07$  meV, the system undergoes a transition to a low-spin ground state. The transitions at these two directions have a different nature, as drawn in the insets. For  $dV > 0$ , the particular quantum dot is deeper and tends to trap more electrons. However, a negative  $dV$  raises the energy cost on the particular quantum well and leads to a lower probability of occupation in a three-electron system. Without the 'mobile' hole in the 'half-filled' system, the ground state becomes a low-spin state instead of a Nagaoka ferromagnetic state.



**Extended Data Fig. 7 | Local energy offsets on all dots.** Same measurement as in Fig. 6, applying the  $\pm 50 \mu\text{eV}$  offset on each of the four dots. Panels correspond to offsets in dots 1 to 4, clockwise from the top left. Note that the asymmetry in the plots is related to the fact that the local energies at point M

are in an asymmetric detuning configuration and we pulse linearly from this configuration to point N. As expected, the simulated energies of the different spin states at point N ( $p_\epsilon = 1$ ), are the same in all four plots.



**ExtendedData Fig. 8 | Large local offsets.** Each pair of panels show experimental measurements (left) and simulated spectra (right), where point N has been redefined such that the chemical potential of dot 1 is offset by the amount shown on the top right of each panel. Green crosses highlight the detuning

points used to obtain the values in Fig. 6b. For experimental plots, these points were obtained using a peak-finding algorithm (local maxima by simple comparison with neighbouring values); for simulated plots, the points correspond to the energy-level crossings.